energies

MDPI

Article

Quantifying Swirl Number Effects on Recirculation Zones and Vortex Dynamics in a Dual-Swirl Combustor

Hafiz Ali Haider Sehole [1,2,†], Ghazanfar Mehdi [1,†], Rizwan Riaz [2,†], Absaar Ul Jabbar [2,†], Adnan Maqsood [2,†] and Maria Grazia De Giorgi [3,†,*]

[1] Department of Mechanical Engineering, School of Engineering, Aalto University, Otakaari 4, 02150 Espoo, Finland; ali.haider@aalto.fi (H.A.H.S.); ghazanfar.mehdi@aalto.fi (G.M.)
[2] School of Interdisciplinary Engineering and Sciences, National University of Sciences and Technology, Islamabad 44000, Pakistan; prorectorric@nust.edu.pk (R.R.); absaar@sines.nust.edu.pk (A.U.J.); adnan@sines.nust.edu.pk (A.M.)
[3] Department of Engineering for Innovation, University of Salento, Via per Monteroni, 73100 Lecce, Italy
* Correspondence: mariagrazia.degiorgi@unisalento.it
† These authors contributed equally to this work.

Abstract

Swirl-stabilized combustors are central to gas turbine technology, where the swirl number critically determines flow structure and combustion stability. This work systematically investigates the isothermal flow in a dual-swirl combustor, focusing on two primary objectives: evaluating advanced turbulence models and quantifying the impact of geometric-induced swirl number variations. Large Eddy Simulation (LES), Detached Eddy Simulation (DES), Scale-Adaptive Simulation (SAS), and the k-ω SST RANS model are compared against experimental data. The results suggest that while all models capture the mean recirculation zones, the scale-resolving approaches (LES, DES, SAS) more accurately predict the unsteady dynamics, such as shear layer fluctuations and the precessing vortex core, which are challenging for the RANS model. Furthermore, a parametric study of vane angles (60° to 70°) reveals a non-monotonic relationship between geometry and the resulting swirl number, attributed to internal flow separation. An intermediate swirl number range ($S \approx 0.79$) was found to promote stable and coherent recirculation zones, whereas higher swirl numbers led to more intermittent flow structures. These findings may provide practical guidance for selecting turbulence models and optimizing swirler geometry in the design of modern combustors.

Keywords: turbulence; swirl number; vortex breakdown

check for updates

Academic Editors: Massimo Masi, Cinzia Tornatore, Simone Salvadori and Pedro Coelho

Received: 2 September 2025
Revised: 3 December 2025
Accepted: 11 December 2025
Published: 16 December 2025

Citation: Sehole, H.A.H.; Mehdi, G.; Riaz, R.; Ul Jabbar, A.; Maqsood, A.; De Giorgi, M.G. Quantifying Swirl Number Effects on Recirculation Zones and Vortex Dynamics in a Dual-Swirl Combustor. *Energies* **2025**, *18*, 6568. https://doi.org/10.3390/en18246568

Copyright: © 2025 by the authors. Licensee MDPI, Basel, Switzerland. This article is an open access article distributed under the terms and conditions of the Creative Commons Attribution (CC BY) license (https://creativecommons.org/licenses/by/4.0/).

1. Introduction

Swirling flows are fundamental to enhancing mixing, heat transfer, and process stability in numerous engineering applications, including reactors, cyclone separators, and, most notably, combustion systems [1,2]. In combustors, swirl is intentionally imparted to the incoming flow to create a robust recirculation zone that stabilizes the flame by recirculating hot combustion products and facilitating efficient fuel–air mixing [3]. Among swirl-generating devices, annular injectors are predominant, often employing a central bluff body or injector to generate diverse and controllable flow patterns [4]. The required swirl strength, controlled by the air-to-fuel ratio and geometric configuration, is key to determining the flame's size and shape.

When the swirl number (S_w), defined as the ratio of tangential to axial momentum, exceeds a critical threshold, vortex breakdown occurs. This phenomenon is characterized by a sudden structural change in the vortex core, severe slowing of axial flow, and the formation of a Central Recirculation Zone (CRZ) along the combustor axis [5–7]. This vortex breakdown manifests in distinct modes; annular swirling jets typically exhibit axisymmetric (bubble), single-helical, and double-helical modes [7]. A critical feature associated with the single-helix mode (Type 2) is the Precessing Vortex Core (PVC), a hydrodynamic instability comprising a helical vortex structure that precesses around the CRZ [8,9]. The PVC significantly enhances turbulent mixing and is therefore crucial for flame stabilization [10,11]. However, its dynamics are complex; while common in non-reactive flows, the PVC can be suppressed or altered when a flame is established [8,12,13].

Accurately predicting these phenomena remains a formidable challenge. The critical swirl number for vortex breakdown is not a universal constant, with reported values varying from 0.45 to 0.94 depending on the specific configuration and measurement methods [2,14,15]. This variation arises because flow dynamics are not determined by the swirl number and initial conditions alone. Outlet boundary conditions have been shown to strongly influence the near-field dynamics of both non-reactive and reactive swirling flows [16–18].

The simulation of these strongly swirling flows presents one of the most difficult aspects of modeling gas turbine combustion. The high flow curvature and adverse pressure gradients inherent in vortex breakdown exacerbate turbulence anisotropy, pushing conventional Reynolds-Averaged Navier–Stokes (RANS) models to their limits [19]. While advanced modeling approaches like Large Eddy Simulation (LES) and hybrid RANS-LES methods (e.g., DES, SAS) offer improved capabilities for capturing transient, large-scale coherent structures like the PVC [20,21], their performance is highly case-dependent. Previous studies have often focused on single-swirl configurations or a limited set of models, leaving a gap in the systematic evaluation of modern turbulence models for predicting the complex flow dynamics in dual-swirl combustors, a design increasingly relevant for low-emission combustion where cold flow patterns are known to dictate subsequent flame behavior [22,23].

The influence of swirl number on combustion dynamics continues to be an area of significant research interest. Recent studies highlight its complex role; for instance, Yellugari et al. [24] observed that higher swirl numbers (>0.7) can cause an upstream shift of the central recirculation zone, potentially increasing flashback risk while also reducing thermal NO_x through enhanced mixing. Similarly, Li et al. [25] reported that an increasing swirl number can modify the recirculation zone geometry and intensify turbulence in single-stage configurations. Further complexity is illustrated by Tang et al. [26], who found that in multi-stage combustors, a specific swirl number (1.5) could help minimize exit temperature distributions. Within this context, the present work aims to contribute by specifically investigating how geometric modifications to the vane angle, under a constant flow rate, influence the resultant swirl number and the ensuing flow structures in a dual-swirl configuration.

This computational study has explored the isothermal flow dynamics within a dual-swirl combustor, focusing on the evaluation of turbulence models and the observed effects of varying the swirl number through geometric modifications. The comparison of turbulence models indicates that while all approaches captured the primary recirculation zones, their performance differed in representing unsteady features. The RANS-based SST model provided a reasonable time-averaged flow field but tended to under-predict turbulence levels and showed limitations in resolving transient dynamics like the Precessing Vortex Core. In comparison, the scale-resolving models (DES, SAS, LES) appeared to offer im-

proved alignment with the unsteady flow physics. The analysis of different vane angles, which produced swirl numbers from 0.7 to 0.94, appeared to reveal distinct flow regimes. The highest swirl number (S = 0.94) resulted in a large Inner Recirculation Zone (IRZ) but an intermittent Outer Recirculation Zone (ORZ), which might present challenges for consistent flame anchoring. The lowest swirl number (S = 0.7) exhibited a more penetrating jet with different stabilization characteristics. The intermediate swirl number (S ≈ 0.79) seemed to strike a favorable balance, producing coherent dual recirculation zones that most closely resembled the experimental reference. This may suggest a potential trade-off in design between jet penetration and recirculation zone robustness. Overall, this work hopes to contribute useful insights for combustor design by illustrating how flow structures respond to geometric changes. The observations around the 65° vane angle and the performance of hybrid turbulence models like DES might offer practical considerations for future studies. These isothermal findings provide a foundation for subsequent investigation of reactive flows, where heat release would introduce additional complexity to the dynamics observed here.

2. Problem Formulation

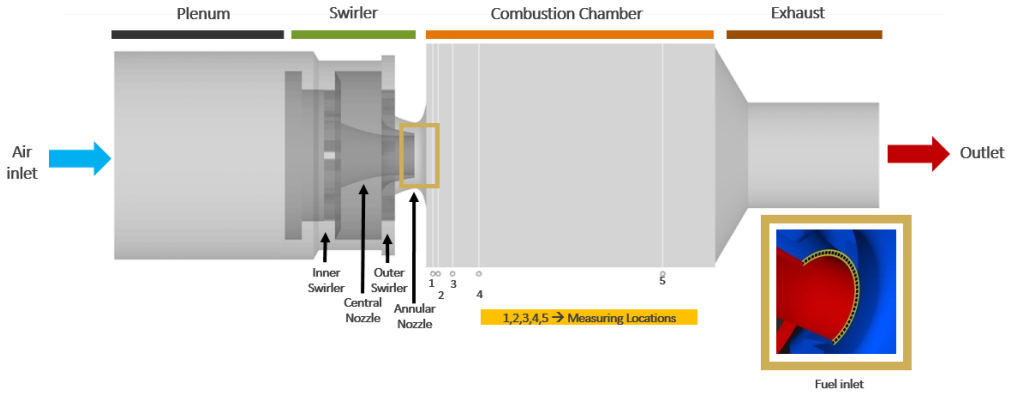
2.1. Computational Setup

This study investigates the isothermal (non-reacting) flow field. The computational setup consists of a dual-swirl combustor, as shown schematically in Figure 1a. The system includes a combustion chamber, plenum, and swirl injector geometry, which was experimentally analyzed by the German Aerospace Center (DLR) [27]. Air enters the combustion chamber from the plenum through the swirl injector at a mass flow rate of 19.74 g/s under ambient conditions using a fixed top-head profile. After passing through the swirl injector, the airflow splits into a ratio of 0.54 between the annular and central passages. Both passages are equipped with vanes aligned at a prescribed angle to the rotation axis, which strongly influences the flow dynamics inside the combustion chamber. In addition to the air supply, fuel as air is introduced through a non-swirling inlet composed of 72 square channels, with a total mass flow rate of 1.256 g/s under ambient conditions using a fixed top head profile. The air and fuel inlet turbulent intensity is 5 per (medium) and 15 per (maximum). The eddy length scale at both inlets is 0.5 mm. The pressure outlet is set to 0 Pa and the operating pressure is 101325 Pa. All walls were treated as adiabatic with no-slip conditions. The corresponding inflow boundary conditions are listed in Table 1.

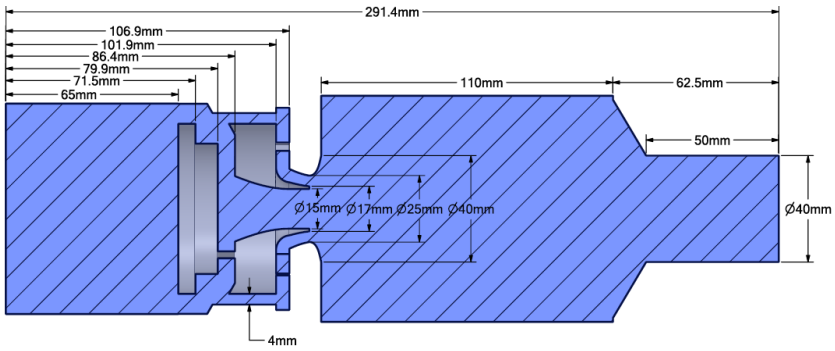
Table 1. Inflow boundary conditions.

Parameter	Value	Description
$\dot{m}$	1.256 g/s	Mass flow rate at fuel inlet
$\dot{m}$	19.74 g/s	Mass flow rate at air inlet

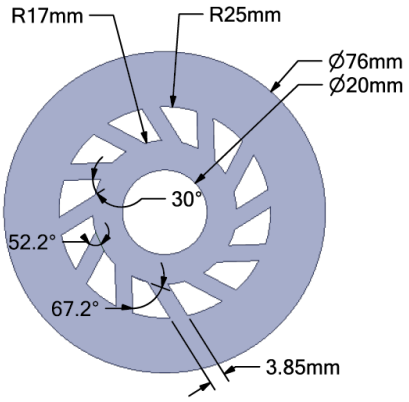
The geometry of the combustor is illustrated in Figure 1b–d. The combustion chamber has a rectangular cross-section with a length of 110 mm and a width of 85 mm. A chimney of 40 mm diameter and 50 mm length is mounted on top of the chamber. The plenum has a diameter of 79 mm and a length of 65 mm. Swirl is imparted by the injector vanes, which are distributed circumferentially at specified angles around the rotation axis. The central injector has a diameter of $d_i = 15$ mm and contains eight radial vanes, while the annular injector has an inner diameter of 17 mm, an outer diameter of 25 mm, and a curved diameter of 40 mm, with 12 radial vanes. The fuel inlet, comprising 72 square channels, has a cross-sectional area of 0.5×0.5 mm^2 each.



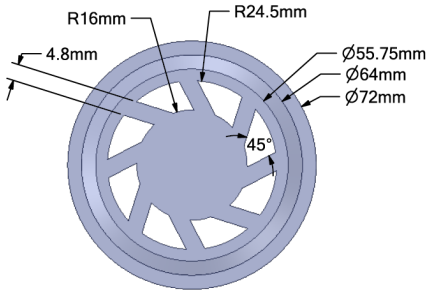
(**a**) Sketch of gas turbine model combustor



(**b**) Important dimensions of gas turbine model combustor



(**c**) Inner Swirler



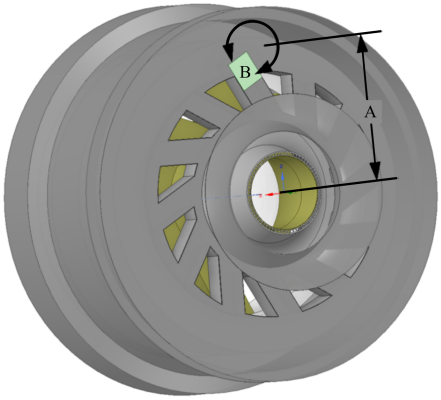
(**d**) Outer swirler

Figure 1. Gas turbine model combustor.

The geometric variation in the Figure 2 is based on a change in the swirl vane angle for both the inner and outer swirlers simultaneously from 60° to 70° across six configurations around the rotational axis. The study is based on a total of six parametric changes. The swirl number calculation is based on the Formula (1) provided in the study of Weigand et al. [28].

$$S = \frac{\int_0^R 2\pi u w \rho r dr}{R \int_0^R 2\pi u^2 \rho r dr} \quad (1)$$

where R is the radius of the annular injector, u is the mean axial velocity, w is the mean tangential velocity, and ρ is the mean density.



Name	A (Length from Origin to Rotation Angel)	B (Rotation Angel)
Mod-1 60	30 mm	60°
Mod-2 62.5	30 mm	62.5°
Mod-3 64	30 mm	64°
Mod-4 65	30 mm	65°
Mod-5 66	30 mm	66°
Mod-6 70	30 mm	70°

Figure 2. Swirl vane orientation. The vane angle θ is measured from the coordinate origin to the rotation center, determining the swirl characteristics.

2.2. Numerical Setup

This study employs a multi-fidelity turbulence modeling approach to systematically evaluate the performance of RANS, hybrid RANS-LES, and LES methods for predicting the complex, unsteady flow in a gas turbine combustor. The models were selected to represent different physical modeling approaches: the SST model (RANS) as the industry standard for steady-state simulations, the DES and SAS models (hybrid RANS-LES) as advanced approaches that aim to resolve large-scale unsteadiness in separated flows, and LES as the highest-fidelity approach that directly resolves the energy-containing turbulent structures. The primary comparative objective is to assess the predictive accuracy of each model for swirling, separated flows under identical numerical conditions, with particular focus on their ability to capture unsteady phenomena and flow structures. A key diagnosis will be to determine whether model inaccuracies stem from physical assumptions (e.g., RANS limitations in inherently unsteady flows), numerical issues, or specific model formulations.

The simulation was carried out using the ANSYS Fluent 16.1 commercial software package with a pressure-based, incompressible-ideal gas law. The reference pressure is set to 101,325 Pa. The coupled pressure-correction scheme was employed to handle the velocity-pressure relationship, while a multi-grid method solved the linear set of coupled equations. All equations were discretized using second-order schemes: a bounded central-difference scheme for momentum in detached flow regions and second-order upwind for other transport equations. The time step size of 1×10^{-5} s was selected to maintain a maximum Courant number below 0.8 throughout the domain, ensuring temporal resolution of turbulent structures. The Courant number is calculated based on the inlet velocity, cell size in the domain (1 mm), and fixed time step of 1×10^{-5}. Statistical convergence was demonstrated by monitoring velocity fluctuations at multiple probe locations over four flow-through times (0.12 s) after initial steady-state establishment, with five inner iterations per time step.

The turbulence models used in this study—Scale Adaptive Simulation (SAS), Detached Eddy Simulation (DES), Large Eddy Simulation (LES), and Shear Stress Transport (SST)—operate on the common principle of the Boussinesq hypothesis to close the Reynolds-averaged or sub-grid stress terms. However, they differ fundamentally in their treatment of turbulent eddies. The RANS-based SST model provides a time-averaged solution, modeling all turbulent scales. In contrast, LES directly resolves the large, energy-containing eddies and only models the smaller, more universal sub-grid scales. The hybrid models, DES and SAS, attempt to blend these approaches: DES explicitly switches from RANS in boundary layers to LES in separated regions based on grid spacing, while SAS dynamically adjusts its

modeled length scale based on the resolved flow field, allowing it to operate in a LES-like mode in unsteady regions.

A critical aspect of this comparative study is the use of a single, consistent computational mesh for all turbulence models. While it is recognized that an ideal LES would typically require a finer mesh, particularly in the boundary layers, and a RANS simulation could be run on a coarser one, this approach allows for a direct and practical comparison of model performance under identical discretization conditions. The selected mesh (described in Section 2.3) was prepare to be sufficient for capturing the essential large-scale turbulent structures and is representative of a mesh that would be used in an industrial design cycle for this class of problem. This methodology tests each model's ability to extract the maximum physical accuracy from a given, constrained computational resource. This setup is particularly challenging for the LES and hybrid models, and any failure to capture the flow physics can be more directly attributed to the model's formulation rather than to mesh inadequacy.

2.2.1. Shear Stress Transport

The Shear Stress Transport (SST) k-ω model [29] is a widely adopted RANS model that combines the robustness of the k-ω model near walls with the free-stream independence of the k-ϵ model in the bulk flow. It is primarily intended for attached boundary layers and mildly separated flows. For the highly swirling and unsteady flows in a combustor, the SST model is expected to provide a time-averaged solution, but it may struggle to accurately capture the large-scale unsteady vortex breakdown and recirculation zones due to its inherent averaging of all turbulent scales.

The SST model builds upon the principle of eddy viscosity and combines the strengths of two turbulence models: the k-ω model and the k-ϵ model. Equations (2) and (3) represent the transport equations for turbulent kinetic energy k and specific dissipation rate ω, respectively.

$$\frac{\partial(\rho k)}{\partial t} + \frac{\partial(\rho \bar{U}_j k)}{\partial x_j} = P_k - \beta^* \rho k \omega + \frac{\partial}{\partial x_j}\left[\left(\mu + \frac{\mu_t}{\tilde{\sigma}_k}\right)\frac{\partial k}{\partial x_j}\right] \tag{2}$$

$$\begin{aligned}\frac{\partial(\rho \omega)}{\partial t} + \frac{\partial(\rho \bar{U}_j \omega)}{\partial x_j} &= \tilde{\alpha}\rho S^2 - \tilde{\beta}\rho\omega^2 + \frac{\partial}{\partial x_j}\left[\left(\mu + \frac{\mu_t}{\tilde{\sigma}_\omega}\right)\frac{\partial \omega}{\partial x_j}\right] \\ &\quad + (1 - F_1)\rho\frac{2}{\sigma_\omega}\frac{\partial k}{\partial x_j}\frac{\partial \omega}{\partial x_j}\end{aligned} \tag{3}$$

In Equation (3), the blending function F_1 provides a smooth transition between the k-ω and k-ϵ turbulence models. The turbulence development in stagnant regions is regulated by the production limiter P_k. The turbulent eddy viscosity is calculated using Equation (4).

$$\mu_t = \frac{a_1 k}{max(a_1\omega, SF_2)} \tag{4}$$

The specific definitions and values for the blending functions, production limiter, and constants utilized in the SST model can be located in Mentor's (1994) study [29]. For the RANS simulations, the Shear Stress Transport (SST) model was used in an unsteady formulation (URANS) to allow for the possibility of capturing large-scale transients, even though its primary strength lies in providing time-averaged solutions [30].

2.2.2. Detached Eddy Simulation Model (DES)

The Detached Eddy Simulation (DES) model, specifically the Strelets formulation based on the SST model [31], is a hybrid RANS-LES approach. Its intended role is to

function as a RANS model within attached boundary layers and as an LES in regions of massive separation, where the grid is sufficiently fine. For the present swirling combustor flow, DES is expected to resolve the unsteady dynamics of the separated central and corner recirculation zones more accurately than SST. A known challenge, addressed by the DDES formulation, is the erroneous activation of LES mode inside the RANS boundary layer (Model Stress Depletion), which can lead to incorrect flow separation.

This study utilized the Strelets model, which combines elements of LES with the two-equation SST-RANS model [31]. The SST-RANS model covers the boundary layer, and the LES model takes over when the turbulent length L_t estimated by the RANS model exceeds the local grid spacing Δ. Unlike the SST model, the turbulent length scale influences the destruction term in the k-ω equation.

$$\frac{\partial(\rho k)}{\partial t} + \frac{\partial(\rho \bar{U}_j k)}{\partial x_j} = P_k - \beta^* \rho k \omega F_{DES} + \frac{\partial}{\partial x_j}\left[\left(\mu + \frac{\mu_t}{\tilde{k}}\right)\frac{\partial k}{\partial x_j}\right] \tag{5}$$

The factor F_{DES} which is the multiplier to the destruction term in Equation (5) is defined as:

$$\begin{aligned} F_{DES} &= \max\left(\frac{L_{t,SST}}{L_{t,DES}}, 1\right), \\ L_{t,SST} &= \frac{\sqrt{k}}{\beta\,\omega}, \\ L_{t,DES} &= C_{DES}\,\Delta. \end{aligned} \tag{6}$$

A zonal DES limiter incorporating the SST turbulence model's blending function is introduced to address grid-induced separation problems [32].

$$F_{DES} = max\left(\frac{L_{t,SST}}{L_{t,DES}}(1 - F_{SST}), 1\right) \tag{7}$$

The model's constants are listed in [31].

2.2.3. Scale Adaptive Simulation Model (SAS)

The Scale Adaptive Simulation (SAS) model [33] is another hybrid RANS-LES approach. Its theoretical basis is the introduction of the von Kármán length scale into the turbulence scale equation, which allows the model to adjust its length scale to the resolved structures. Unlike DES, the SAS transition is not explicitly grid-dependent but is triggered by flow instabilities. For swirling flows, SAS is intended to provide a RANS solution in stable shear layers while resolving the unsteady spectrum of turbulence in regions of inherent unsteadiness, such as the precessing vortex core.

The SAS model is based on the k-kL formulation by Menter and Egorov [33]. This integration results in a modified transport equation for the specific dissipation rate in the SST model:

$$\begin{aligned} \frac{\partial(\rho\omega)}{\partial t} + \frac{\partial \rho \bar{U}_j}{\omega}\partial x_j = \tilde{\sigma}\rho\S^2 - \tilde{\beta}\rho\omega^2 + \frac{\partial}{\partial x_j}\left[\frac{\mu_t}{\tilde{\sigma}_\omega}\frac{\partial\omega}{\partial x_j}\right] \\ + \frac{2\rho}{\sigma_\phi}\frac{1}{\omega}\frac{\partial k}{\partial x_j}\frac{\partial\omega}{\partial x_j} + F_{SAS-SST} \end{aligned} \tag{8}$$

The additional term is given by (9);

$$F_{SAS-SST} = -\frac{2\rho}{\sigma_\phi}\frac{k}{\omega^2}\frac{\partial\omega}{\partial x_j}\frac{\partial\omega}{\partial x_j} + \tilde{\zeta}_2\kappa\rho S^2\frac{L}{L_{vk}} \tag{9}$$

2.2.4. Large Eddy Simulation

The Large Eddy Simulation (LES) approach directly resolves the large, energy-containing eddies and models the effect of the smaller, sub-grid scales. It represents the highest fidelity level used in this study and is theoretically the most suitable for capturing the unsteady, swirling, and separated flow dynamics in the combustor. Its predictive role is to serve as a benchmark for the other models. The primary limitation in this comparative study is the use of a single mesh, which may not be fully sufficient for a wall-resolved LES, potentially leading to modeling inaccuracies in the near-wall region.

The LES employs the WALE subgrid-scale model [34]. The WALE model has been widely used to predict complex turbulence phenomena in gas turbine combustors [35–38]. Hence, the WALE model is also used for the 3D test cases studied herein. In the WALE model, the subgrid viscosity is given as

$$\nu_t = (C_w \Delta)^2 \frac{(\mathcal{S}_{ij}^d \mathcal{S}_{ij}^d)^{3/2}}{(\tilde{S}_{ij}\tilde{S}_{ij})^{5/2} + (\mathcal{S}_{ij}^d \mathcal{S}_{ij}^d)^{5/4}}, \tag{10}$$

where the strain rate tensor is defined $\tilde{S}_{ij} = \frac{1}{2}(\partial \tilde{u}_i/\partial x_j + \partial \tilde{u}_j/\partial x_i)$, model constant $C_w = 0.325$, Δ is the filter width and

$$\mathcal{S}_{ij}^d = \frac{1}{2}\left(\frac{\partial \tilde{u}_i}{\partial x_k}\frac{\partial \tilde{u}_k}{\partial x_j} + \frac{\partial \tilde{u}_j}{\partial x_k}\frac{\partial \tilde{u}_k}{\partial x_i}\right) + \frac{1}{3}\frac{\partial \tilde{u}_k}{\partial x_m}\frac{\partial \tilde{u}_m}{\partial x_k}\delta_{ij}. \tag{11}$$

2.3. Mesh Generation

The mesh resolution is critical for capturing the relevant physical phenomena in turbulent flow simulations and its the same mesh as used in sehole at al. [39] The computational mesh consists of 12.7 million cells with a global base size of 1.0 mm and a refined minimum cell size of 0.2 mm around the fuel inlets, utilizing tetrahedral elements with octree refinement and structured-like stacking in critical regions. In this study, the mesh adequacy was assessed using the integral length scale (L_t), which characterizes the size of the most energy-containing turbulent eddies. The integral length scale is calculated from RANS SST precursor simulations as:

$$L_t = \frac{k^{3/2}}{\varepsilon} \tag{12}$$

where k is the turbulent kinetic energy and ε is the turbulent dissipation rate. The mesh resolution requirement was determined by the ratio L_t/Δ, where Δ represents the local grid cell size. To ensure proper resolution of the dominant turbulent structures, the mesh was assessed to maintain $L_t/\Delta \geq 5$ in the regions of concern, which corresponds to resolving at least 80% of the turbulent kinetic energy by capturing eddies larger than $L_t/2$. Figure 3 shows the spatial distribution of L_t/Δ, with values of 5 or higher in critical regions indicating well-resolved large eddies [40,41]. The near-wall resolution was characterized by the non-dimensional wall distance y^+, with a maximum value of 24.6 along the combustion chamber wall [39], which is appropriate for wall-modeled simulations where shear-driven flows dominate the combustion chamber dynamics.

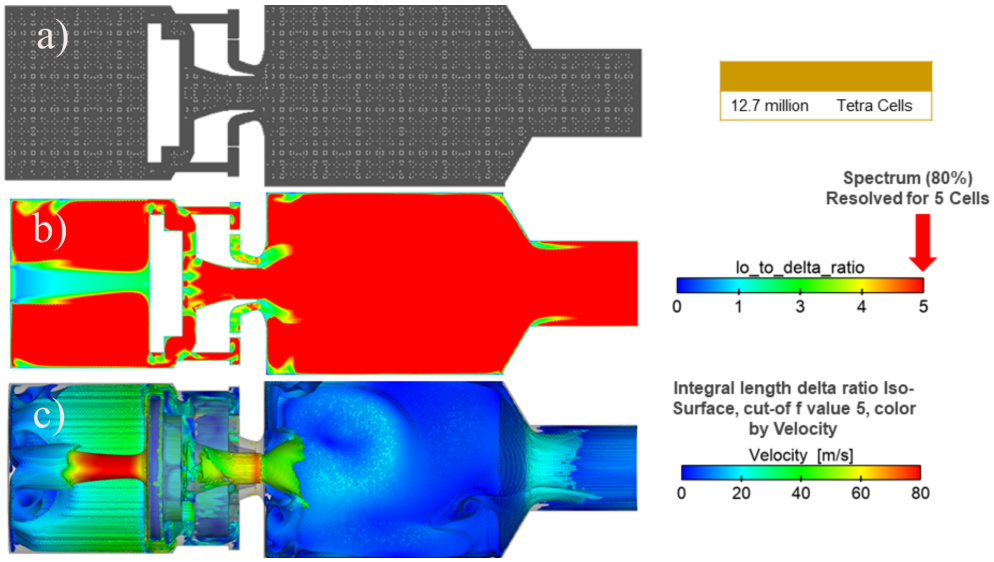


Figure 3. Computational mesh and resolution analysis. (**a**) Top: Overview of the computational grid used for all simulations. (**b**) Middle: Contour plot of the ratio of integral length scale to grid spacing (L_t/Δ), indicating regions where turbulent structures are adequately resolved ($L_t/\Delta \geq 5$). (**c**) Bottom: Iso-surface of the integral length scale colored by velocity magnitude, showing the distribution of energy-containing turbulent eddies throughout the domain.

3. Results and Discussion

This work aims to explore two main areas. First, it seeks to evaluate the performance of several turbulence modeling approaches (RANS, DES, SAS, and LES) in simulating the complex flow within a dual-swirl configuration under isothermal conditions. This initial step, which builds upon our earlier work on reactive flows [39], is intended to help validate the numerical methodology and better isolate hydrodynamic effects from those of heat release. The second objective is to examine how geometric changes, specifically to the swirl vane angle and the resulting swirl number, influence the resulting flow patterns and turbulence. It is hoped that this combined approach can contribute to the computational guidelines for predicting these flows and offer some useful insights into the behavior of modern dual-swirl combustors.

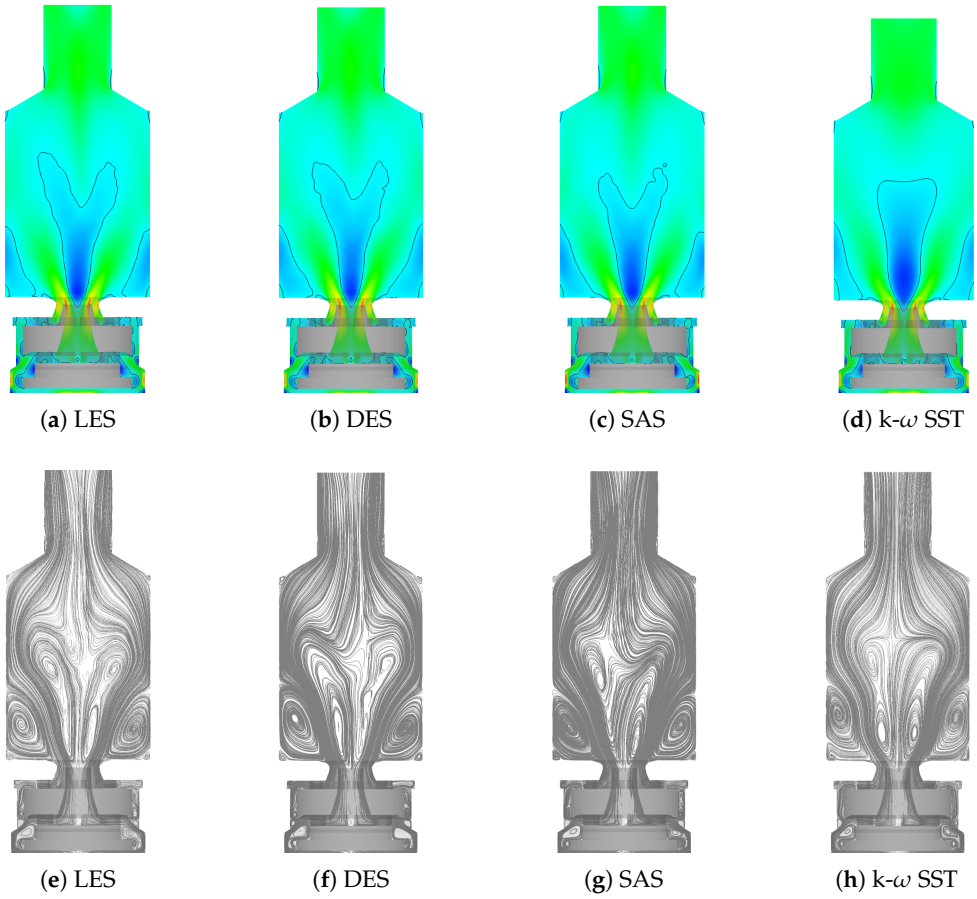
3.1. Part 1: Numerical Investigation of Turbulence Models

The numerical domain is described in Section 2.1, focusing on the mod 4-65 swirl angle configuration shown in Figure 2. For this comparative study, four common turbulence modeling approaches were selected: LES, DES, SAS, and k-omega SST. Following conventional practice, the data presented relies on time-averaged quantities. This averaging was performed over a period of four residence times, which began only after the flow had reached a statistically steady state, a process that took approximately two residence times; the total simulation time was 0.12 s.

3.1.1. General Flow Structure

Figure 4 depicts the time-averaged general flow structures, which represent the dominant flow patterns over time. This figure presents a two-dimensional plane with a mean axial velocity contour and corresponding streamlines. The black solid lines highlight the mean axial velocity stagnation points and two key flow features: the inner recirculation zone (IRZ) and the outer recirculation zone (ORZ). These zones are understood to form due to vortex breakdown of the swirling flow from the injector. The IRZ is concentric with the central injector, while the ORZ appears near the chamber's corners. The streamlines illustrate the complex flow field, which is typically stabilized in enclosed swirl burners

with a concentric inflow. Consistent with expectations for such configurations, the time-averaged flow field shows the presence of both the IRZ and ORZ. Although the combustion chamber has a square geometry, the time-averaged flow field appears largely axisymmetric; however, some deviations from perfect symmetry can be observed in numerical data. These flow structures are highly turbulent, and their size and position fluctuate periodically. The region between the two recirculation zones is where fresh gas is expected to enter the combustion chamber.



(**a**) LES (**b**) DES (**c**) SAS (**d**) k-ω SST

(**e**) LES (**f**) DES (**g**) SAS (**h**) k-ω SST

Figure 4. Time-averaged axial velocity contours ((**top**) row) and corresponding streamlines ((**bottom**) row) for different turbulence models. Black lines indicate recirculation zone boundaries (axial velocity = 0 m/s). All plots share common scales: axial velocity range −10 to 40 m/s, spatial coordinates in mm.

The simulation results indicate an average inner recirculation zone (IRZ) length of approximately 60 mm and a maximum width of 40 mm. The IRZ appears to penetrate nearly 4 mm into the central injector. An outer recirculation zone (ORZ) is present in the chamber corners. Between these zones, two shear layers form, sandwiching a fresh stream of air and fuel. The shear layer between the IRZ and the fresh stream is highly turbulent, with significant velocity gradients and fluctuations observed at their interface. The recirculation zones are inherently unsteady, with their size and shape fluctuating over time. Additional, smaller recirculation zones are noted at the annular injector exit, the top corners of the chamber, and the exhaust injector exit, likely caused by sudden geometric expansions. The injector geometry also splits the air mass flow rate at a ratio of 0.54, a value that appears consistent across all turbulence models tested.

A comparison of the LES, DES, SAS, and k-ω SST models shows that while all capture the primary recirculation zones, the k-ω SST model as URANS, produces a different IRZ

shape. This is a known limitation of linear eddy-viscosity URANS models in strongly swirling flows. Even in an unsteady mode, the model's inherent time-averaging approach and elevated turbulent viscosity dampen unsteady fluctuations and diffuse the shear layer, preventing the resolution of highly coherent, anisotropic structures such as the Precessing Vortex Core (PVC) [19]. Consequently, even on a relatively fine mesh, the k-ω SST model does not fully resolve the transient vortex breakdown process in the way that the scale-resolving models (DES, SAS, LES) do.

3.1.2. Time-Averaged and RMS Measurements

Figure 5 presents the time-averaged velocity components at various heights within the combustion chamber, corresponding to the measurement locations of 2.5 mm, 5 mm, 10 mm, 20 mm, and 90 mm shown in Figure 1b. In the axial velocity profiles, a sharp gradient is observed where the fresh air and fuel stream enters the chamber, with a peak value of approximately 35 m/s at the 2.5 mm height. The radial velocity component appears more pronounced within the outer recirculation zone (ORZ), which is consistent with an inward-directed flow, particularly at distances greater than 10 mm along the curve. Its magnitude is roughly half that of the axial component. The tangential velocity profile shows notable variations across the shear layer between the IRZ and ORZ, remaining relatively constant within the ORZ itself.

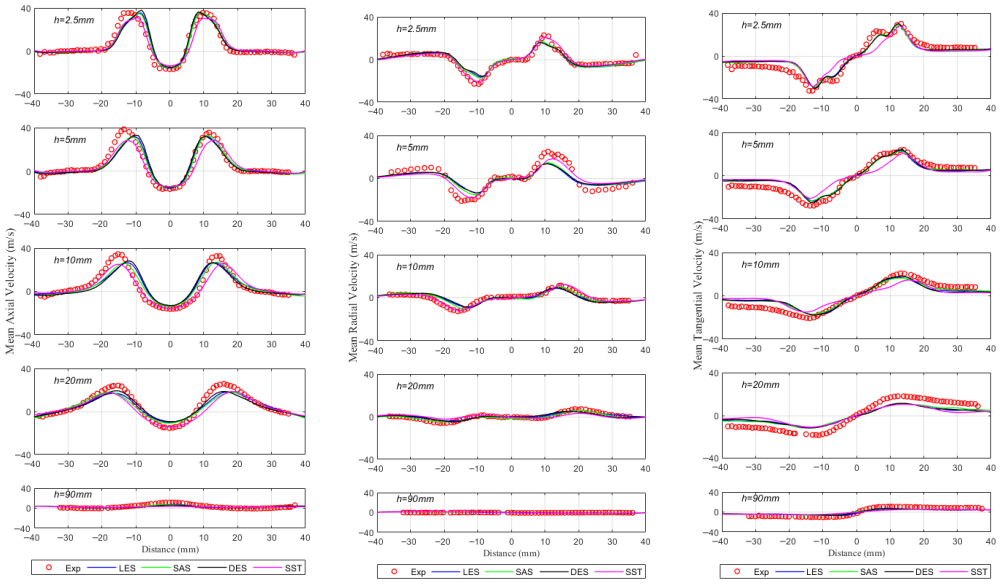


Figure 5. Time-averaged velocity profiles at five chamber heights (2.5, 5, 10, 20, 90 mm): axial (**left**), radial (**middle**), and tangential (**right**) components. Red circles represent LDA measurements; colored lines show numerical predictions. Axes: velocity (m/s) vs. radial position (mm).

At the 5 mm and 10 mm heights, the behavior of the velocity components aligns with the patterns visible in the contour plot of the mean axial velocity (Figure 4). Further downstream at 20 mm, the velocity magnitudes generally decrease, and the ORZ contracts. Near the outlet, at the 90 mm height, the radial velocity component diminishes significantly, likely due to flow contraction from the outlet geometry, accompanied by a corresponding increase in the axial and tangential components.

Figure 5 also allows for a comparison of these results across different turbulence models (LES, DES, SAS, and k-ω SST). The scale-resolving models—LES, DES, and SAS—show generally similar performance. Among them, LES and DES capture higher peak velocities and similar recirculation patterns (Figure 4e,f), with DES showing slightly higher peaks than LES. The k-ω SST model, while following the overall trend of the experimental data, tends to underperform in regions of high shear. Specifically, it appears to under-predict the

axial velocity and over-predict the radial component, and it does not capture the strength of the shear layer as effectively as the scale-resolving models. These observations suggest that the sub-grid models may be better suited for capturing the complex, unsteady dynamics in this swirl-stabilized flow.

Figure 6 presents the turbulent velocity fluctuations (RMS values). The highest axial velocity fluctuations are observed in the shear layers between the IRZ and ORZ, with peak values reaching approximately 17 m/s within the IRZ. Similarly, radial velocity fluctuations appear more pronounced in the IRZ compared to the ORZ, which may indicate a region of intensive mixing. The ORZ itself shows dominant radial velocity fluctuations over its axial and tangential components. Tangential velocity fluctuations remain relatively constant throughout the ORZ but undergo sharp transitions across the shear layers. Overall, the flow field demonstrates higher turbulence levels near the inlet, gradually decreasing toward the chamber outlet, with minor peaks persisting along the rotation axis and near the chamber walls.

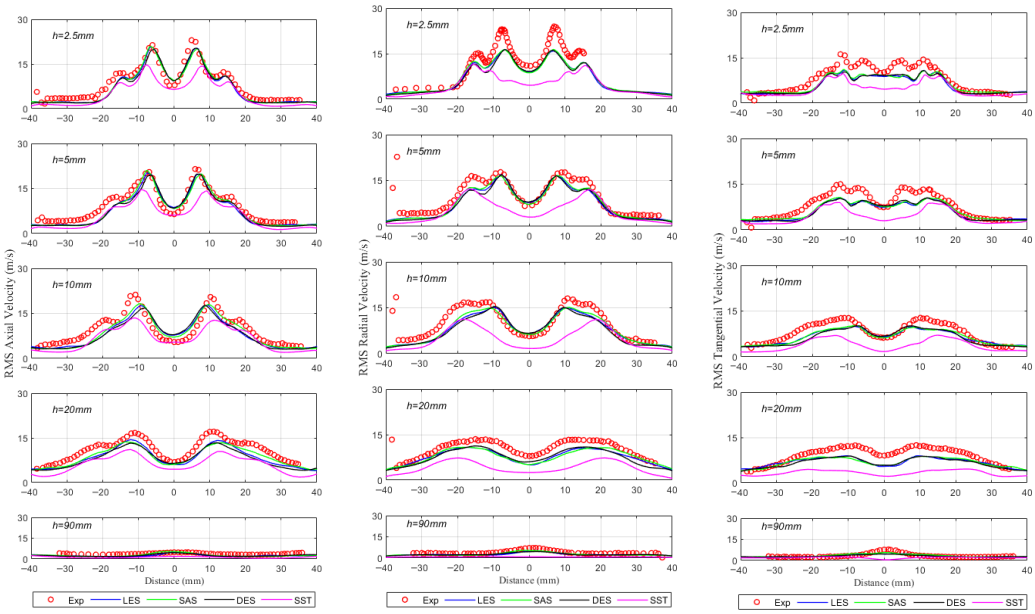


Figure 6. Root mean square (RMS) velocity fluctuations at five chamber heights: axial (**left**), radial (**middle**), and tangential (**right**) components. Red circles represent LDA measurements; colored lines show numerical predictions. Axes: velocity fluctuation (m/s) vs. radial position (mm).

All the scale-resolving models appear to capture the main trends in turbulent fluctuations across all velocity components. In contrast, the k-ω SST model seems to struggle to capture the higher RMS values. This shortcoming likely stems from the model's fundamental assumption of isotropic turbulence, which makes it difficult to represent the energy contained in large-scale, organized motions like a precessing vortex core (PVC). This finding suggests a key practical insight: for predicting unsteady mixing and instability phenomena in swirl combustors, a scale-resolving model (such as DES, SAS, or LES) may be necessary, even on a mesh not specifically optimized for LES. Among these scale-resolving models, DES and LES show a slightly better capture of peak fluctuations compared to SAS in this configuration, indicating their potential for stronger performance under these practical constraints.

A statistical comparison of the turbulence models is provided in Table 2, which details the maximum and centerline values for mean and RMS velocities at each measurement location. The data suggest that the scale-resolving approaches—LES, SAS, and DES—generally show closer agreement with the experimental (Exp.) results. The differences in mean axial

velocity between these models and the experiment are typically on the order of 1–2 m/s at most locations, indicating a consistent performance.

In contrast, the RANS model (k-ω SST) shows larger deviations, with differences in mean axial velocity ranging from approximately 4 to 10 m/s across the various chamber locations. Furthermore, a more pronounced discrepancy is observed in the RMS values, where the k-ω SST model consistently under-predicts the velocity fluctuations. This pattern, evident across all velocity components, underscores the greater challenge this model faces in capturing the flow's unsteady dynamics.

Table 2. Comparison of Maximum and Centerline Velocity Metrics: Time-Averaged (Mean) and Fluctuation (RMS) Values for Axial, Radial, and Tangential Components. Values are presented for the Mod-4 (65°) configuration, comparing experimental measurements (Exp) against predictions from Large Eddy Simulation (LES), Detached Eddy Simulation (DES), Scale-Adaptive Simulation (SAS), and the k-ω SST model.

		Axial Velocity (m/s)				**Radial Velocity (m/s)**				**Tangential Velocity (m/s)**			
Loc.	**Method**	**Mean Max**	**Mean Center**	**RMS Max**	**RMS Center**	**Mean Max**	**Mean Center**	**RMS Max**	**RMS Center**	**Mean Max**	**Mean Center**	**RMS Max**	**RMS Center**
2.5 mm	Exp	35.44	−16.84	22.98	7.86	22.79	−0.13	23.94	10.95	30.04	0.52	16.15	10.20
	LES	36.07	−15.97	20.66	9.42	16.80	−0.13	16.42	8.89	29.98	0.20	10.87	8.81
	SAS	35.56	−15.51	20.92	9.57	16.68	0.72	16.43	8.69	28.61	−0.36	11.16	9.14
	DES	37.97	−15.19	20.33	9.32	15.85	−0.36	16.33	9.17	29.89	−0.28	10.75	9.19
	SST	31.11	−13.58	14.69	6.49	21.17	−0.24	11.45	4.60	28.04	−0.23	9.85	4.63
5 mm	Exp	38.47	−16.50	21.49	6.45	24.99	1.95	22.75	6.93	23.93	0.00	15.00	7.42
	LES	32.33	−15.94	20.21	8.69	14.26	−0.11	17.00	7.75	23.22	0.32	10.57	7.38
	SAS	32.86	−15.38	21.04	8.34	14.74	0.77	16.72	7.17	22.47	−0.62	10.72	7.63
	DES	33.01	−15.15	19.77	8.46	13.68	−0.33	16.93	7.95	24.10	−0.07	10.54	7.89
	SST	28.37	−14.45	14.64	6.11	18.33	−0.13	12.34	3.04	20.62	−0.13	8.99	3.04
10 mm	Exp	34.40	−16.04	21.25	5.47	11.46	0.90	18.46	5.68	20.77	0.52	12.76	6.24
	LES	26.73	−13.31	17.72	7.73	8.76	−0.27	15.14	6.65	16.92	−0.29	9.95	6.55
	SAS	27.08	−13.84	18.23	7.11	10.51	−0.11	15.14	6.28	16.34	−0.43	10.22	6.27
	DES	28.03	−12.88	17.56	7.91	9.23	0.35	15.41	6.68	17.92	0.30	10.15	6.76
	SST	25.70	−15.41	13.49	5.42	12.16	−0.07	11.27	1.70	14.58	−0.07	7.07	1.72
20 mm	Exp	25.80	−15.40	17.12	6.90	7.22	−0.38	13.51	7.95	18.03	0.52	12.47	9.03
	LES	18.29	−10.06	14.40	6.10	5.97	−0.53	10.78	5.07	10.65	−0.45	8.97	5.46
	SAS	18.08	−10.79	13.67	6.11	5.95	−1.72	10.83	5.13	11.12	−0.12	8.77	5.88
	DES	19.25	−9.39	13.38	6.49	4.98	0.11	11.28	6.05	11.40	−0.19	8.86	5.82
	SST	18.53	−14.31	11.08	4.49	3.13	−0.25	7.32	2.48	10.46	0.13	4.57	2.21
90 mm	Exp	11.52	11.18	4.86	4.86	0.23	−0.26	7.12	7.07	10.94	−2.05	7.82	7.66
	LES	7.81	7.59	5.04	4.97	1.59	−0.85	5.27	5.07	7.49	−2.69	4.85	4.48
	SAS	7.54	7.44	5.51	5.39	1.15	−0.53	5.40	5.32	6.75	0.94	5.66	5.65
	DES	6.18	6.16	4.48	4.48	1.59	0.26	4.58	4.44	6.46	−0.65	4.64	4.64
	SST	3.81	3.60	2.63	1.89	1.43	−0.23	0.91	0.87	5.16	−0.39	2.65	0.52

Notes: 1. **Mean Max** = Maximum value of mean velocity profile. **Mean Center** = Mean velocity at radial centerline (r = 0). **RMS Max** = Maximum RMS value (peak turbulence intensity). **RMS Center** = RMS value at radial centerline (r=0). 2. All values in m/s. Velocity components: Axial (U), Radial (V), Tangential (W). 3. Exp = Experimental, LES = Large Eddy Simulation, SAS = Scale-Adaptive Simulation, DES = Detached Eddy Simulation, SST = Shear Stress Transport. 4. Near-injector locations (2–10 mm) show highest turbulence intensities in both mean and RMS profiles.

3.2. Part 2: Effect of Swirl Number on Flow Dynamics

This work explores how geometric control of the swirl number, through modifications to the vane angle, influences flow stability and turbulence in a dual-swirl configuration. While prior research has established that coherent flow structures are affected by the swirl number, equivalence ratio, and geometry [8], the present study focuses specifically on isolating the effect of the vane angle. By maintaining a constant equivalence ratio, this

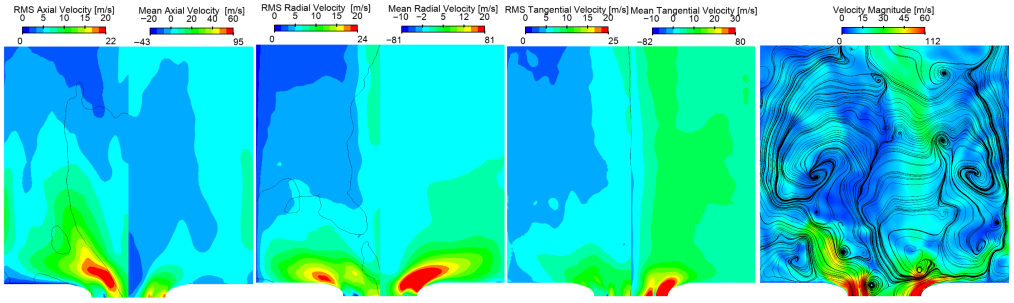
work attempts to quantify the relationship between the vane angle, the resulting swirl number, and key flow parameters such as recirculation zone stability, turbulence intensity, and mixing effectiveness.

For the parametric study, the Detached Eddy Simulation (DES) model was selected. This choice was made after initial validation showed that the scale-resolving models (LES, SAS, and DES) all demonstrated a strong and comparable ability to capture the key flow physics, with none exhibiting a consistent, decisive advantage across all metrics (Table 2). Given this parity, DES was chosen for its well-established hybrid formulation, which offers a practical balance between computational efficiency in attached boundary layers and the resolution of larger turbulent structures in separated flow regions. This balance made DES a suitable candidate for the extensive computations required for a geometric parameter sweep.

The swirl number, a dimensionless metric characterizing rotational intensity in fluid flow, is defined as the ratio of axial flux of tangential momentum to axial flux of axial momentum. In this study, it was evaluated at the outlet of each swirler module. The time-averaged flow was analyzed for vane angles ranging from 60° to 70°. The resulting swirl numbers for each configuration are presented in Table 3, with corresponding flow fields visualized in Figures 7–12. Table 3 indicates a non-monotonic relationship between vane angle and the resulting swirl number. A notable decrease is observed between 64° (S = 0.86) and 65° (S = 0.787). This behavior may be attributed to the onset of flow separation within the swirler passages; as the vane angle increases beyond a critical point, the adverse pressure gradient can lead to separation, reducing effective flow turning and tangential momentum imparted to the flow. The slight recovery at 66° (S = 0.793) could suggest a change in the separation pattern. This finding underscores that the geometric vane angle alone does not directly dictate the swirl number, as the internal flow behavior and potential separation must also be considered. The physical implications of these varying swirl numbers are reflected in the velocity data of Table 4. For instance, the 65° and 66° configurations, which have similar swirl numbers (0.79), also show comparable mean axial velocities near the inlet (e.g., 38 m/s at 2.5 mm), suggesting a consistent underlying flow structure. In contrast, the 70° vane, with the lowest swirl number (S = 0.7), exhibits a significantly different flow, characterized by a much weaker central recirculation (less negative Mean Center axial velocity at 2.5 mm and 9.5 mm) and higher turbulence levels (RMS) further downstream. The flow fields in Figures 7–12 provide visual confirmation of these trends, showing measurable differences in recirculation zone structure that align with the quantitative data. Collectively, these results illustrate how vane angle—through its effect on swirl number—influences the resulting flow patterns and turbulence. This understanding may contribute to better-informed design of fuel injectors for combustion systems.

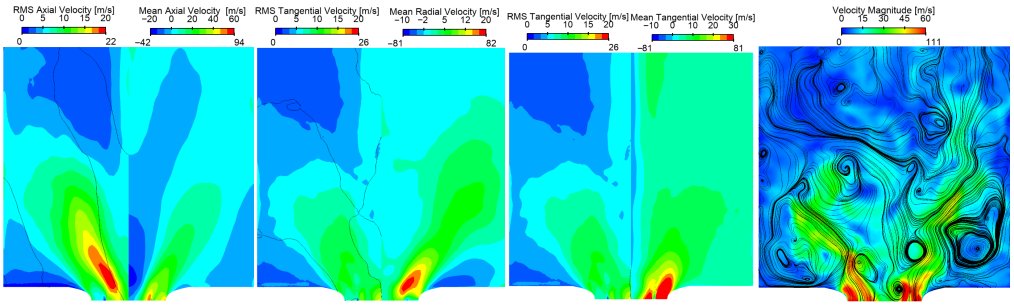
Table 3. Swirl Number Variations with Geometric Modifications.

Swirl Number	Geometric Modification	Vane Angle
0.94	Mod-1	60°
0.88	Mod-2	62.5°
0.86	Mod-3	64°
0.787	Mod-4	65°
0.793	Mod-5	66°
0.7	Mod-6	70°



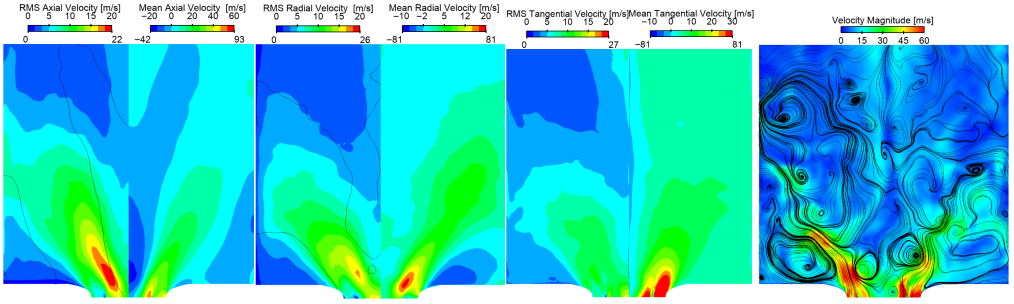
(**a**) Axial (**b**) Radial (**c**) Tangential (**d**) Instantaneous

Figure 7. Mod-1 (60°): Contour plots showing (**a**) axial, (**b**) radial, and (**c**) tangential velocity components (time-averaged with RMS contours overlaid). Panel (**d**) displays instantaneous velocity magnitude with streamlines.



(**a**) Axial (**b**) Radial (**c**) Tangential (**d**) Instantaneous

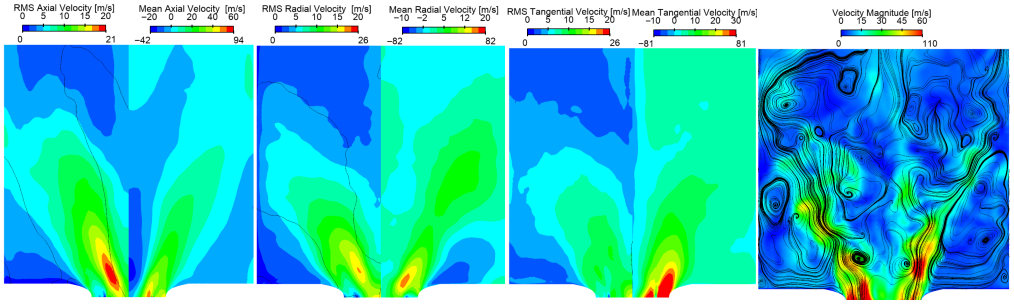
Figure 8. Mod-1 (62.5°): Contour plots showing (**a**) axial, (**b**) radial, and (**c**) tangential velocity components (time-averaged with RMS contours overlaid). Panel (**d**) displays instantaneous velocity magnitude with streamlines.



(**a**) Axial (**b**) Radial (**c**) Tangential (**d**) Instantaneous

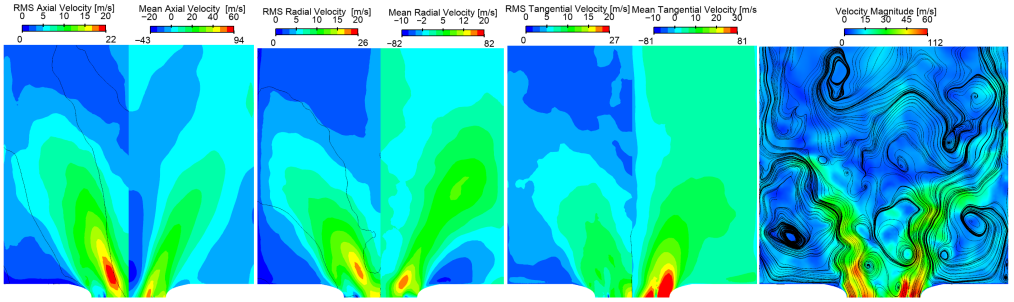
Figure 9. Mod-1 (64°): Contour plots showing (**a**) axial, (**b**) radial, and (**c**) tangential velocity components (time-averaged with RMS contours overlaid). Panel (**d**) displays instantaneous velocity magnitude with streamlines.

The time-averaged flow fields for vane angles ranging from 60° to 70° are presented in Table 3 and visualized in Figures 7–12. Each contour plot displays the mean velocity components, RMS components, and instantaneous velocity magnitude for a given geometric module. In the time-averaged plots, the boundaries of the recirculation zones are indicated by the black line corresponding to zero axial velocity. In the instantaneous plots, solid black lines represent velocity streamlines. This labeling convention is used consistently throughout this work to identify key features.



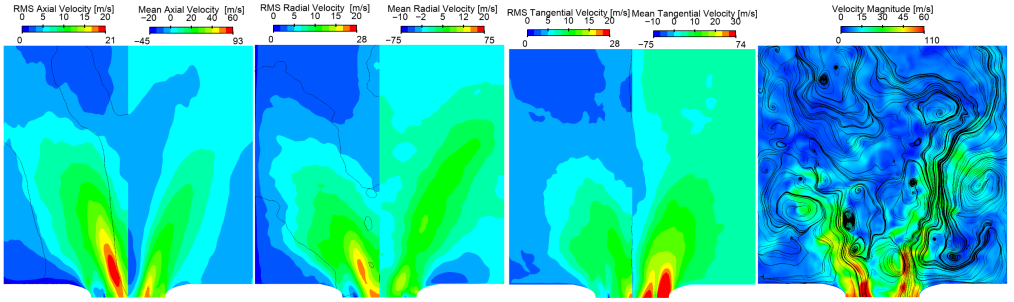
(**a**) Axial (**b**) Radial (**c**) Tangential (**d**) Instantaneous

Figure 10. Mod-1 (65°): Contour plots showing (**a**) axial, (**b**) radial, and (**c**) tangential velocity components (time-averaged with RMS contours overlaid). Panel (**d**) displays instantaneous velocity magnitude with streamlines.



(**a**) Axial (**b**) Radial (**c**) Tangential (**d**) Instantaneous

Figure 11. Mod-1 (66°): Contour plots showing (**a**) axial, (**b**) radial, and (**c**) tangential velocity components (time-averaged with RMS contours overlaid). Panel (**d**) displays instantaneous velocity magnitude with streamlines.



(**a**) Axial (**b**) Radial (**c**) Tangential (**d**) Instantaneous

Figure 12. Mod-1 (70°): Contour plots showing (**a**) axial, (**b**) radial, and (**c**) tangential velocity components (time-averaged with RMS contours overlaid). Panel (**d**) displays instantaneous velocity magnitude with streamlines.

As seen in Figures 7–12, an increase in swirl number generally correlates with the formation of a larger vortex breakdown bubble and enhanced jet spreading. The flow structure of Mod-1 (60°) differs significantly from the others, characterized by a larger, differently shaped inner recirculation zone (IRZ) and the absence of a well-defined outer recirculation zone (ORZ), which is replaced by smaller recirculation areas in the combustor corners. For the other modules, as the vane angle increases from 62.5° to 70°, the IRZ appears to contract and move upward while the ORZ expands, as quantified in Figure 13. These changes are influenced by the shifting balance between swirler inflow and outlet backflow. The stability of the IRZ, which is a key factor for flame anchoring [42], is thus influenced by these geometric modifications.

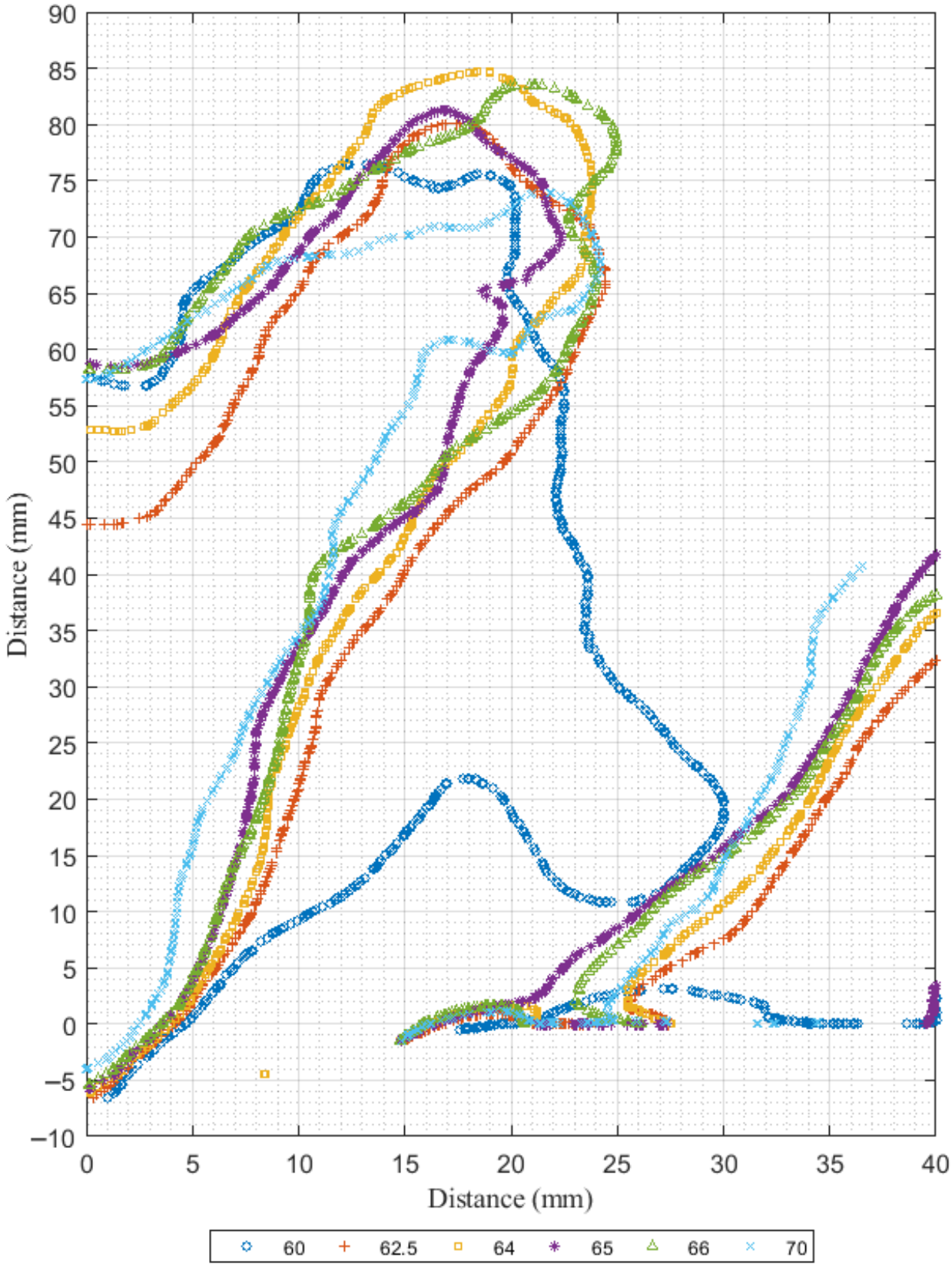


Figure 13. Recirculation zones identified by the zero contour of mean axial velocity. The inner recirculation zone (IRZ) and outer recirculation zones (ORZ) are visualized, showing the flow reversal regions critical for flame stabilization in the swirling combustor flow.

Figure 14 shows the time-averaged velocity components at five heights within the chamber (see Figure 1b), compared against experimental data for reference. The maximum predicted velocities at the 2.5 mm location for each module are detailed in Table 4. In general, as the swirl number increases from 0.7 to 0.94, the dominance of the axial and tangential velocities decreases due to jet spreading, while the radial component becomes more influential. This is particularly evident in Mod-1, where the high radial velocity component correlates with its unique IRZ and the lack of a stable ORZ. The axial and radial velocities primarily determine the global flow features, while the tangential velocity significantly influences the IRZ penetration. A higher tangential velocity leads to an IRZ that penetrates into the central injector, whereas a lower tangential velocity results in an IRZ situated above the fuel inlets, as illustrated in Figure 2.

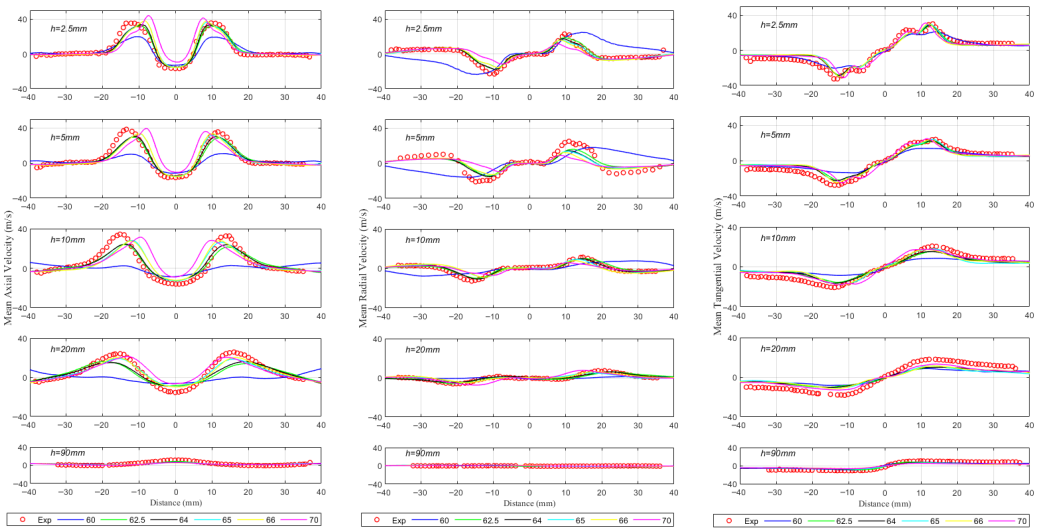


Figure 14. Comparison of time-averaged velocity profiles for different swirl vane configurations (Mod-1 to Mod-6): axial (**left**), radial (**center**), and tangential (**right**) components at five axial positions. Experimental measurements obtained via Laser Doppler Anemometry (LDA) are shown as red circles.

Figure 15 presents the root mean square (RMS) values of velocity components, calculated at five axial heights within the combustion chamber (see Figure 1b), with experimental data provided for reference. At the 2.5 mm measurement location, the maximum RMS values across the modules (Mod-1 to Mod-6) show axial components of 21.43, 20.92, 21.14, 19.87, 20.19, and 20.00 m/s; radial components of 15.45, 16.62, 16.69, 16.33, 17.02, and 17.02 m/s; and tangential components of 11.51, 11.30, 11.37, 10.75, 10.35, and 12.13 m/s, respectively. The highest axial and radial fluctuations appear in Mod-1, while the maximum tangential fluctuation occurs in Mod-6. These elevated RMS values appear to originate from the shear layer between the inner recirculation zone (IRZ) and the incoming flow, where large velocity gradients and low mean velocities seem to promote higher turbulent intensity. The observed ratio of mean axial velocity to its RMS value significantly exceeds 100% in this region, suggesting potential for intense mixing between fresh gas and burned products from the IRZ. This may indicate that Mod-1, Mod-2, and Mod-3 could experience relatively higher mixing rates compared to other configurations. The broad peaks in radial RMS profiles around 6 mm further suggest strong flow unsteadiness in the shear layer, while the absence of a defined second shear layer in Mod-1 around 20 mm distinguishes its flow characteristics from other cases where this feature appears between the inflow and outer recirculation zone.

Table 4. Quantitative maximum and centerline velocity metrics from the swirl vane parametric study. Tabulated values show time-averaged and RMS velocity components, with experimental LDA measurements provided for the baseline configuration.

		Axial Velocity (m/s)				**Radial Velocity (m/s)**				**Tangential Velocity (m/s)**			
Loc.	**Angle**	**Mean Max**	**Mean Center**	**RMS Max**	**RMS Center**	**Mean Max**	**Mean Center**	**RMS Max**	**RMS Center**	**Mean Max**	**Mean Center**	**RMS Max**	**RMS Center**
2.5 mm	Exp	35.44	−16.84	22.98	7.86	22.79	−0.13	23.94	10.95	30.04	0.52	16.15	10.20
	60°	19.69	−13.04	21.43	8.39	24.69	0.43	18.45	8.75	21.18	−1.74	11.51	9.06
	62.5°	32.24	−15.50	21.26	8.86	18.75	0.21	16.62	8.53	28.47	0.30	11.48	8.61
	64°	33.49	−15.74	21.14	8.88	17.24	−0.50	16.69	8.10	28.81	−0.24	11.37	8.41
	65°	37.97	−15.19	20.33	9.32	15.85	−0.36	16.33	9.17	29.89	−0.28	10.75	9.19
	66°	37.94	−15.83	20.19	9.59	16.00	−0.20	17.15	9.03	30.10	−0.07	10.35	9.07
	70°	44.04	−9.46	20.00	12.23	11.24	0.03	17.06	12.00	31.06	−1.06	12.13	12.12
10 mm	Exp	38.47	−16.50	21.49	6.45	24.99	1.95	22.75	6.93	23.93	0.00	15.00	7.42
	60°	10.79	−11.52	19.03	7.72	17.95	−0.07	15.52	7.76	13.88	−1.76	10.33	8.07
	62.5°	29.38	−14.85	20.16	8.12	15.90	0.15	16.72	7.21	22.12	0.01	10.65	7.05
	64°	30.53	−15.10	20.00	8.23	14.39	−0.39	16.88	6.79	22.20	−0.02	10.56	7.19
	65°	33.01	−15.15	19.77	8.46	13.68	−0.33	16.93	7.95	24.10	−0.07	10.54	7.89
	66°	33.23	−15.62	19.66	8.59	12.28	−0.01	17.82	7.91	23.46	−0.64	10.10	7.68
	70°	39.38	−10.51	20.38	11.27	8.92	−0.18	17.52	11.20	24.73	−0.20	11.28	11.28
15 mm	Exp	34.40	−16.04	21.25	5.47	11.46	0.90	18.46	5.68	20.77	0.52	12.76	6.24
	60°	6.18	−8.63	16.28	7.06	7.73	−0.45	10.66	6.98	8.55	−1.42	8.17	6.20
	62.5°	23.83	−12.44	18.49	7.42	10.08	0.42	15.10	6.16	15.42	−0.96	10.27	5.91
	64°	24.47	−12.72	18.33	7.13	9.91	−0.03	15.02	5.61	15.34	0.15	10.01	5.96
	65°	28.03	−12.88	17.56	7.91	9.23	0.35	15.41	6.68	17.92	0.30	10.15	6.76
	66°	27.87	−12.20	16.67	7.52	7.99	0.19	16.08	6.52	17.30	−0.03	9.99	6.69
	70°	31.38	−9.05	18.31	9.55	5.90	−0.07	15.91	10.06	17.57	0.84	11.27	9.78
20 mm	Exp	25.80	−15.40	17.12	6.90	7.22	−0.38	13.51	7.95	18.03	0.52	12.47	9.03
	60°	10.34	−6.27	11.65	6.94	1.26	−1.19	7.22	7.20	8.61	−0.73	6.19	5.69
	62.5°	16.27	−8.35	14.87	6.39	6.20	−0.43	10.63	5.91	10.07	−0.90	8.87	6.11
	64°	15.99	−9.42	14.39	6.54	6.12	0.47	10.79	5.17	9.97	−0.41	8.99	5.00
	65°	19.25	−9.39	13.38	6.49	4.98	0.11	11.28	6.05	11.40	−0.19	8.86	5.82
	66°	20.26	−9.76	13.57	6.16	6.43	0.25	11.13	5.80	11.31	−0.40	8.74	5.17
	70°	21.30	−6.57	14.71	7.99	7.66	−0.80	11.08	7.45	13.24	0.08	9.94	7.55
90 mm	Exp	11.52	11.18	4.86	4.86	0.23	−0.26	7.12	7.07	10.94	−2.05	7.82	7.66
	60°	6.71	6.59	5.76	5.75	1.58	1.08	7.50	7.47	8.42	1.48	8.21	8.07
	62.5°	8.71	8.68	6.36	6.22	1.58	−1.24	6.84	6.60	8.32	−1.51	6.29	6.23
	64°	6.39	6.38	4.86	4.54	1.08	0.64	5.61	5.49	6.91	−0.39	6.73	6.73
	65°	6.18	6.16	4.48	4.48	1.59	0.26	4.58	4.44	6.46	−0.65	4.64	4.64
	66°	5.60	5.59	3.85	3.80	1.51	1.47	4.54	4.51	5.82	0.28	4.18	4.18
	70°	5.93	5.93	4.17	4.10	0.95	0.15	4.76	4.58	5.71	0.12	4.67	4.56

Notes: 1. **Mean Max** = Maximum value of mean velocity profile. **Mean Center** = Mean velocity at radial centerline (r = 0). **RMS Max** = Maximum RMS value (peak turbulence intensity). **RMS Center** = RMS value at radial centerline (r = 0). 2. All values in m/s. Velocity components: Axial (U), Radial (V), Tangential (W). 3. Exp = Experimental, Angles = Injection angle parameter study. 4. Critical region: 7–14.5 mm shows highest sensitivity to injection angle changes. 5. 65°–66° angles show best agreement with experimental data across most metrics.

The relationship between vane angle and the resulting flow dynamics, as quantified in Tables 3 and 4, provides insight into the stability of the recirculation zones. The distinct velocity profiles for the 60° and 70° vane angles are a direct consequence of their respective swirl numbers (S = 0.94 and S = 0.7) relative to the critical threshold for vortex breakdown. While a swirl number of 0.7 indeed represents a strongly swirling flow, it appears to be at or near the lower limit for establishing the classical vortex breakdown structure observed in the higher-swirl cases. In Mod-60 (S = 0.94), the very high swirl number generates an intense radial pressure gradient, leading to a robust vortex breakdown. This manifests as a large, coherent Inner Recirculation Zone (IRZ) that significantly impedes the axial flow, resulting in the lowest axial velocities (e.g., 19.69 m/s at 2.5 mm). The flow energy is instead partitioned into strong tangential motion and, as the flow expands, a dominant radial velocity component. In contrast, Mod-70 (S = 0.7), while still a strong swirl, produces a weaker radial pressure gradient. This results in a less pronounced vortex breakdown and a shallower, weaker IRZ, offering less resistance to the axial jet. This explains the significantly higher axial velocities (44.04 m/s at 2.5 mm). The flow exhibits less radial spreading, leading to lower radial velocities, while the tangential velocity remains high but is insufficient to generate the same level of recirculation as in Mod-60. Therefore, the data illustrates a critical transition in flow topology. The configurations around 65°–66° (S ≈ 0.79) achieve a balance that best replicates the experimental benchmark. Mod-60 (S = 0.94) exhibits a flow dominated by recirculation and expansion, while Mod-70 (S = 0.7), despite its strong swirl, produces a flow regime where the axial jet momentum is more preserved, leading to higher penetration but a potentially less stable flame-anchoring region.

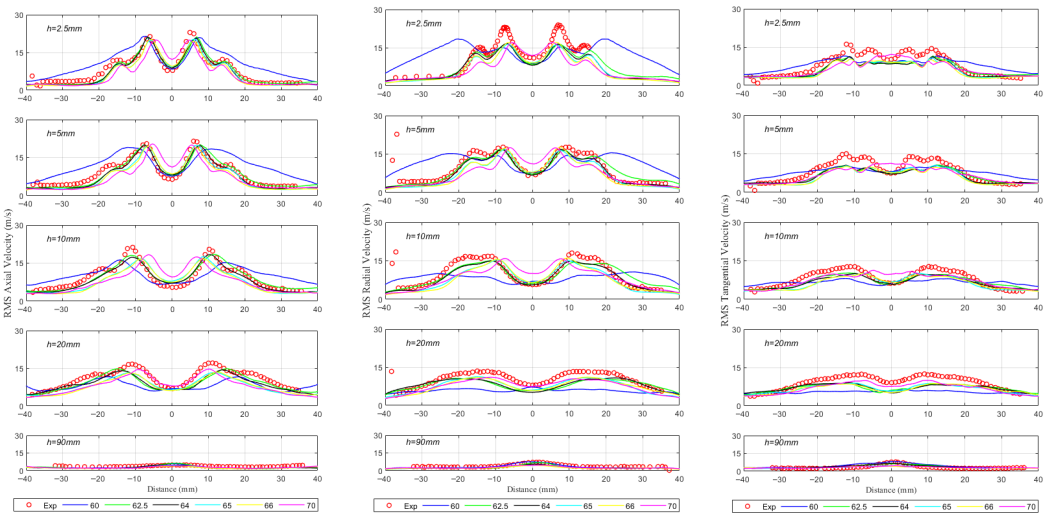


Figure 15. Comparison of root mean square (RMS) velocity fluctuations across different swirl vane configurations (Mod-1 to Mod-6): axial (**left**), radial (**center**), and tangential (**right**) components. Experimental LDA measurements (red circles) provide validation at multiple chamber heights.

While time-averaged data offer valuable insights into mean flow characteristics, they may not fully represent the complex, unsteady structures that govern combustion chamber dynamics, as illustrated in Figure 16. The instantaneous flow is characterized by a V-shaped swirl gas inflow, where surface streamlines reveal small-scale, transient vortices along the inner and outer shear layers, some of which appear to originate deep within the central injector. The presence of these structures, combined with high turbulence intensity between the shear layers, seems to promote intense mixing between the cold fresh gas and the hot products recirculated from the IRZ and ORZ. This suggests that flame stabilization, often attributed to large recirculation zones, may in fact rely on a collection of smaller,

unsteady recirculation pockets rather than the single, coherent IRZ typically depicted in time-averaged representations.

Further analysis of the vortical structures, highlighted by pressure iso-surfaces, indicates that the inner shear layer exhibits a zig-zag arrangement rather than a uniform height, a pattern that appears to strengthen with increasing radial distance. This arrangement may signal the presence of a Precessing Vortex Core (PVC), a feature known to be unstable in both non-reacting and reacting flows, particularly at high swirl numbers. The helical structure associated with the PVC is not captured in time-averaged fields due to its transient nature. The observed instabilities generated by this precessing motion are understood to influence swirling motions significantly, which could play an important role in mixing and combustion processes central to swirling flame dynamics.

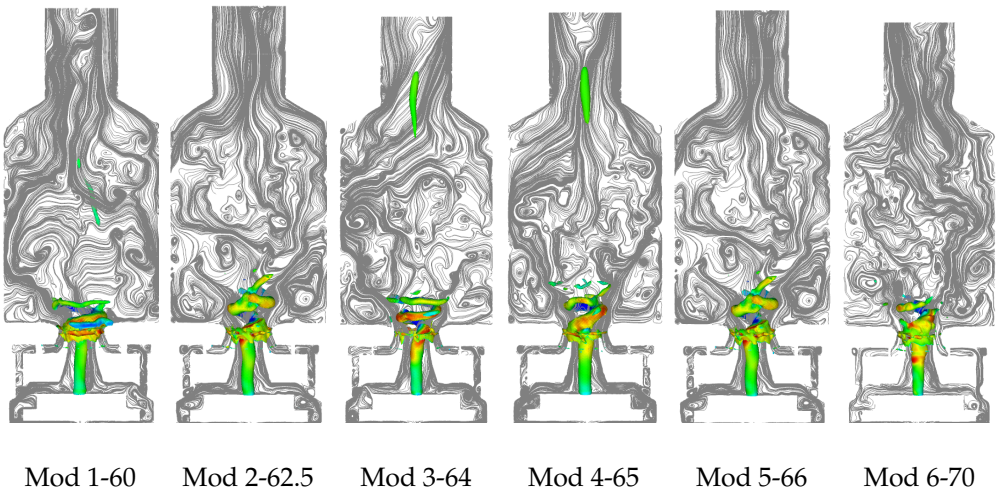


Figure 16. Instantaneous flow field characterization: Velocity streamlines (gray) and pressure iso-surfaces (colored) showing the development of coherent structures across different swirl vane angles (Mod-1 to Mod-6). The helical patterns indicate strong PVC activity, particularly at higher swirl numbers.

4. Conclusions

This computational study has sought to explore the isothermal flow dynamics within a dual-swirl combustor, with a focus on evaluating turbulence models and understanding the effects of swirl number variations controlled by vane geometry.

The comparison of turbulence models suggests that while all models capture the main recirculation zones, their performance varies in predicting unsteady features. The RANS-based SST model, while providing a useful time-averaged representation, tended to under-predict turbulence levels and struggled to resolve transient shear layer dynamics and the Precessing Vortex Core (PVC). In comparison, the scale-resolving approaches (DES, SAS, LES) appeared to offer a closer agreement with the unsteady physics. This suggests that for predicting key unsteady phenomena, hybrid methodologies may be suitable as well.

The analysis of swirl number effects, achieved by varying vane angles from 60° to 70°, provided several observations. A non-monotonic relationship was noted between the geometric vane angle and the resulting swirl number, potentially due to flow separation within the swirler passages. The results also indicated different flow regimes: a high-swirl condition (S = 0.94) with a large IRZ and less stable ORZ, a low-swirl condition (S = 0.7) with a more penetrating jet, and an intermediate range (S $\approx$ 0.79) that seemed to promote stable dual recirculation zones which aligned well with experimental data.

In summary, this work attempts to contribute to combustor design by offering quantitative insights into the flow response to geometric changes. The results may suggest that a vane angle near 65° could provide a favorable balance for this configuration, and that

hybrid models like DES can be a practical tool for simulating such complex flows. These isothermal findings provide a foundation, and future work investigating reactive flows would be a valuable next step to understand the interplay with combustion.

Author Contributions: Conceptualization, H.A.H.S. and R.R.; Methodology, H.A.H.S., R.R., A.U.J., G.M., M.G.D.G. and A.M.; Software, H.A.H.S.; Validation, H.A.H.S.; Formal analysis, H.A.H.S.; Resources, R.R.; Data curation, G.M.; Writing—original draft, H.A.H.S.; Writing—review and editing, G.M., M.G.D.G., A.M. and R.R.; Supervision, R.R.; Funding acquisition, G.M. and M.G.D.G. All authors have read and agreed to the published version of the manuscript.

Funding: This research received no external funding

Data Availability Statement: The original contributions presented in this study are included in the article. Further inquiries can be directed to the corresponding authors.

Acknowledgments: The authors acknowledge the computational support provided by the Supercomputing Facility at SINES, NUST, Islamabad. G.M. acknowledges the support provided by the Merenkulun Säätiö / Maritime Foundation Finland (Grant No. 20250056) and COST Action CA22151, Cyber-Physical Systems and Digital Twins for the Decarbonization of Energy-Intensive Industries (CYPHER).

Conflicts of Interest: The authors declare no conflicts of interest.

References

1. Syred, N.; Beér, J. Combustion in swirling flows: A review. *Combust. Flame* **1974**, *23*, 143–201. [CrossRef]
2. Gupta, A.K.; Lilley, D.G.; Syred, N. Swirl flows. In *Tunbridge Wells*; Abacus Press: London, UK, 1984.
3. Chterev, I.; Emerson, B.; Lieuwen, T. Velocity and stretch characteristics at the leading edge of an aerodynamically stabilized flame. *Combust. Flame* **2018**, *193*, 92–111. [CrossRef]
4. Davies, T.; Beér, J. Flow in the wake of bluff-body flame stabilizers. *Symp. (Int.) Combust.* **1971**, *13*, 631–638. [CrossRef]
5. Leibovich, S. The structure of vortex breakdown. *Annu. Rev. Fluid Mech.* **1978**, *10*, 221–246. [CrossRef]
6. Escudier, M. Vortex breakdown: Observations and explanations. *Prog. Aerosp. Sci.* **1988**, *25*, 189–229. [CrossRef]
7. Lucca-Negro, O.; O'Doherty, T. Vortex breakdown: A review. *Prog. Energy Combust. Sci.* **2001**, *27*, 431–481. [CrossRef]
8. Syred, N. A review of oscillation mechanisms and the role of the precessing vortex core (PVC) in swirl combustion systems. *Prog. Energy Combust. Sci.* **2006**, *32*, 93–161. [CrossRef]
9. Yazdabadi, P.; Griffiths, A.; Syred, N. Characterization of the PVC phenomena in the exhaust of a cyclone dust separator. *Exp. Fluids* **1994**, *17*, 84–95. [CrossRef]
10. Anacleto, P.; Fernandes, E.; Heitor, M.; Shtork, S. Swirl flow structure and flame characteristics in a model lean premixed combustor. *Combust. Sci. Technol.* **2003**, *175*, 1369–1388. [CrossRef]
11. Zhang, R.; Boxx, I.; Meier, W.; Slabaugh, C.D. Coupled interactions of a helical precessing vortex core and the central recirculation bubble in a swirl flame at elevated power density. *Combust. Flame* **2019**, *202*, 119–131. [CrossRef]
12. Oberleithner, K.; Terhaar, S.; Rukes, L.; Oliver Paschereit, C. Why nonuniform density suppresses the precessing vortex core. *J. Eng. Gas Turbines Power* **2013**, *135*, 121506. [CrossRef]
13. Roux, S.; Lartigue, G.; Poinsot, T.; Meier, U.; Bérat, C. Studies of mean and unsteady flow in a swirled combustor using experiments, acoustic analysis, and large eddy simulations. *Combust. Flame* **2005**, *141*, 40–54. [CrossRef]
14. Panda, J.; McLaughlin, D. Experiments on the instabilities of a swirling jet. *Phys. Fluids* **1994**, *6*, 263–276. [CrossRef]
15. Toh, I.K.; Honnery, D.; Soria, J. Axial plus tangential entry swirling jet. *Exp. Fluids* **2010**, *48*, 309–325. [CrossRef]
16. Escudier, M.; Keller, J. Recirculation in swirling flow-a manifestation of vortex breakdown. *AIAA J.* **1985**, *23*, 111–116. [CrossRef]
17. Altgeld, H.; Jones, W.; Wilhelmi, J. Velocity measurements in a confined swirl driven recirculating flow. *Exp. Fluids* **1983**, *1*, 73–78. [CrossRef]
18. Gilchrist, R.; Naughton, J. Experimental study of incompressible jets with different initial swirl distributions: Mean results. *AIAA J.* **2005**, *43*, 741–751. [CrossRef]
19. Sloan, D.G.; Smith, P.J.; Smoot, L. Modeling of swirl in turbulent flow systems. *Prog. Energy Combust. Sci.* **1986**, *12*, 163–250. [CrossRef]
20. Müller, S.; Kleiser, L. Large-eddy simulation of vortex breakdown in compressible swirling jet flow. *Comput. Fluids* **2008**, *37*, 844–856. [CrossRef]

21. Oberleithner, K.; Sieber, M.; Nayeri, C.N.; Paschereit, C.O.; Petz, C.; Hege, H.C.; Noack, B.R.; Wygnanski, I. Three-dimensional coherent structures in a swirling jet undergoing vortex breakdown: Stability analysis and empirical mode construction. *J. Fluid Mech.* **2011**, *679*, 383–414. [CrossRef]
22. Vanoverberghe, K.P.; Van Den Bulck, E.V.; Tummers, M.J. Confined annular swirling jet combustion. *Combust. Sci. Technol.* **2003**, *175*, 545–578. [CrossRef]
23. Vanierschot, M. Fluid Mechanics and Control of Annular Jets With and Without Swirl. Ph.D. Thesis, Vrije Universiteit Brussel, Brussels, Belgium, 2007.
24. Yellugari, K.; Villalva Gomez, R.; Gutmark, E. Effects of Swirl Number and Central Rod on Flow in a Lean Premixed Swirl Combustor. *Combust. Sci. Technol.* **2025**, *197*, 999–1027. [CrossRef]
25. Liang, H.; Maxworthy, T. An experimental investigation of swirling jets. *J. Fluid Mech.* **2005**, *525*, 115–159. [CrossRef]
26. Tang, C.; Li, J.; Jin, W.; Yuan, L.; Yao, Q. Numerical investigation on the influence of swirl number to high-temperature zone evolution and outlet temperature distribution in multi-stage combustor. *Fuel* **2025**, *381*, 133264. [CrossRef]
27. Widenhorn, A.; Noll, B.; Aigner, M. Numerical characterization of a gas turbine model combustor. In *High Performance Computing in Science and Engineering'09*; Springer: Berlin/Heidelberg, Germany, 2010; pp. 179–195.
28. Weigand, P.; Meier, W.; Duan, X.R.; Stricker, W.; Aigner, M. Investigations of swirl flames in a gas turbine model combustor: I. Flow field, structures, temperature, and species distributions. *Combust. Flame* **2006**, *144*, 205–224. [CrossRef]
29. Menter, F.R. Two-equation eddy-viscosity turbulence models for engineering applications. *AIAA J.* **1994**, *32*, 1598–1605. [CrossRef]
30. Wilcox, D.C. *Turbulence Modeling for CFD*; DCW industries: La Canada, CA, USA, 1998; Volume 2.
31. Strelets, M. Detached eddy simulation of massively separated flows. In Proceedings of the 39th Aerospace Sciences Meeting and Exhibit, Reno, NV, USA, 8–11 January 2001; p. 879.
32. Noll, B.; Schütz, H.; Aigner, M. Numerical simulation of high-frequency flow instabilities near an airblast atomizer. In Proceedings of the Turbo Expo: Power for Land, Sea, and Air, New Orleans, LA, USA, 4–7 June 2001; American Society of Mechanical Engineers: New York, NY, USA, 2001; Volume 78514, p. V002T02A008.
33. Menter, F.; Egorov, Y. A scale adaptive simulation model using two-equation models. In Proceedings of the 43rd AIAA Aerospace Sciences Meeting and Exhibit, Reno, NV, USA, 10–13 January 2005; p. 1095.
34. Nicoud, F.; Ducros, F. Subgrid-scale stress modelling based on the square of the velocity gradient tensor. *Flow Turbul. Combust.* **1999**, *62*, 183–200. [CrossRef]
35. Palulli, R.; Dybe, S.; Zhang, K.; Güthe, F.; Alemela, P.R.; Paschereit, C.O.; Duwig, C. Characterisation of non-premixed, swirl-stabilised, wet hydrogen/air flame using large eddy simulation. *Fuel* **2023**, *350*, 128710. [CrossRef]
36. Strempfl, P.; Dounia, O.; Laera, D.; Poinsot, T. Effects of mixing assumptions and models for LES of hydrogen-fueled rotating detonation engines. *Int. J. Hydrogen Energy* **2024**, *62*, 1–16. [CrossRef]
37. Dillon, S.; Mercier, R.; Fiorina, B. Controlling the resolved flame thickness of non-premixed flames in LES with filtered tabulated chemistry. *Proc. Combust. Inst.* **2024**, *40*, 105294. [CrossRef]
38. Zhang, K.; Shen, Y.; Palulli, R.; Ghobadian, A.; Nouri, J.; Duwig, C. Combustion characteristics of steam-diluted decomposed ammonia in multiple-nozzle direct injection burner. *Int. J. Hydrogen Energy* **2023**, *48*, 16083–16099. [CrossRef]
39. Sehole, H.A.H.; Mehdi, G.; Riaz, R.; Maqsood, A. Investigation of Sustainable Combustion Processes of the Industrial Gas Turbine Injector. *Processes* **2025**, *13*, 960. [CrossRef]
40. Fluent, A. *Fluent 14.0 User's Guide*; Ansys Fluent Inc.: Canonsburg, PA, USA, 2011.
41. Pope, S.B. Turbulent flows. *Meas. Sci. Technol.* **2001**, *12*, 2020. [CrossRef]
42. Widenhorn, A.; Noll, B.; Aigner, M. Accurate boundary conditions for the numerical simulation of thermoacoustic phenomena in gas-turbine combustion chambers. In Proceedings of the Turbo Expo: Power for Land, Sea, and Air, Barcelona, Spain, 8–11 May 2006; Volume 42363, pp. 347–356.

Disclaimer/Publisher's Note: The statements, opinions and data contained in all publications are solely those of the individual author(s) and contributor(s) and not of MDPI and/or the editor(s). MDPI and/or the editor(s) disclaim responsibility for any injury to people or property resulting from any ideas, methods, instructions or products referred to in the content.